

Predicting Solar Cell Performance from Terahertz and Microwave Spectroscopy

Hempel, Hannes; Savenjie, Tom J.; Stolterfoht, Martin; Neu, Jens; Failla, Michele; Paingad, Vaisakh C.; Kužel, Petr; Zhao, Jiashang; Siebbeles, Laurens D.A.; More Authors

DOI

[10.1002/aenm.202102776](https://doi.org/10.1002/aenm.202102776)

Publication date

2022

Document Version

Final published version

Published in

Advanced Energy Materials

Citation (APA)

Hempel, H., Savenjie, T. J., Stolterfoht, M., Neu, J., Failla, M., Paingad, V. C., Kužel, P., Zhao, J., Siebbeles, L. D. A., & More Authors (2022). Predicting Solar Cell Performance from Terahertz and Microwave Spectroscopy. *Advanced Energy Materials*, 12(13), Article 2102776. <https://doi.org/10.1002/aenm.202102776>

Important note

To cite this publication, please use the final published version (if applicable).
Please check the document version above.

Copyright

Other than for strictly personal use, it is not permitted to download, forward or distribute the text or part of it, without the consent of the author(s) and/or copyright holder(s), unless the work is under an open content license such as Creative Commons.

Takedown policy

Please contact us and provide details if you believe this document breaches copyrights.
We will remove access to the work immediately and investigate your claim.

Predicting Solar Cell Performance from Terahertz and Microwave Spectroscopy

Hannes Hempel,* Tom J. Savenjie, Martin Stolterfoht, Jens Neu, Michele Failla, Vaisakh C. Paingad, Petr Kužel, Edwin J. Heilweil, Jacob A. Spies, Markus Schleuning, Jiashang Zhao, Dennis Friedrich, Klaus Schwarzburg, Laurens D.A. Siebbeles, Patrick Dörflinger, Vladimir Dyakonov, Ryuzi Katoh, Min Ji Hong, John G. Labram, Maurizio Monti, Edward Butler-Caddle, James Lloyd-Hughes, Mohammad M. Taheri, Jason B. Baxter, Timothy J. Magnanelli, Simon Luo, Joseph M. Cardon, Shane Ardo, and Thomas Unold

Dedicated to the memory of Charles A. Schmuttenmaer


Mobilities and lifetimes of photogenerated charge carriers are core properties of photovoltaic materials and can both be characterized by contactless terahertz or microwave measurements. Here, the expertise from fifteen laboratories is combined to quantitatively model the current-voltage characteristics of a solar cell from such measurements. To this end, the impact of measurement conditions, alternate interpretations, and experimental inter-laboratory variations are discussed using a (Cs,FA,MA)Pb(I,Br)₃ halide perovskite thin-film as a case study. At 1 sun equivalent excitation, neither transport nor recombination is significantly affected by exciton formation or trapping. Terahertz, microwave, and photoluminescence transients for the neat material yield consistent effective lifetimes implying a resistance-free JV-curve with a potential power conversion efficiency of 24.6 %. For grainsizes above ≈ 20 nm, intra-grain charge transport is characterized by terahertz sum mobilities of $\approx 32 \text{ cm}^2 \text{ V}^{-1} \text{ s}^{-1}$. Drift-diffusion simulations indicate that these intra-grain mobilities can slightly reduce the fill factor of perovskite solar cells to 0.82, in accordance with the best-realized devices in the literature. Beyond perovskites, this work can guide a highly predictive characterization of any emerging semiconductor for photovoltaic or photoelectrochemical energy conversion. A best practice for the interpretation of terahertz and microwave measurements on photovoltaic materials is presented.

1. Introduction

For applications of semiconductor materials in, for example, photovoltaics, solar fuel cells, and light-emitting diodes, large charge carrier mobilities are desirable to enable efficient charge injection and extraction, while in microelectronics, the achievable data processing speed is ultimately limited by charge carrier mobilities. Long non-radiative lifetimes are required for large open-circuit voltages or high luminescence quantum yields in devices. Therefore, charge carrier mobilities and lifetimes are metrics for the quality of a semiconducting material and are widely used to guide the development of more efficient devices. Both properties can be probed in a contactless manner by Time-Resolved Microwave Conductivity (TRMC) experiments and Optical-Pump Terahertz-Probe (OPTP) spectroscopy, which makes them excellent tools for the characterization of photovoltaic materials.

H. Hempel, T. Unold
Department of Structure and Dynamics of Energy Materials
Helmholtz-Zentrum Berlin für Materialien und Energie
Hahn-Meitner-Platz 1 14109, Berlin, Germany
E-mail: hannes.hempel@helmholtz-berlin.de

T. J. Savenjie, M. Failla, J. Zhao, L. D.A. Siebbeles
Optoelectronic Materials Section
Department of Chemical Engineering
Delft University of Technology
Van der Maasweg 9, Delft 2629 HZ, The Netherlands

 The ORCID identification number(s) for the author(s) of this article can be found under <https://doi.org/10.1002/aenm.202102776>.

© 2022 The Authors. Advanced Energy Materials published by Wiley-VCH GmbH. This is an open access article under the terms of the Creative Commons Attribution License, which permits use, distribution and reproduction in any medium, provided the original work is properly cited.

DOI: 10.1002/aenm.202102776

M. Stolterfoht
Institute of Physics and Astronomy
University of Potsdam
14467, Potsdam, Germany

J. Neu
Department of Molecular Biophysics and Biochemistry and Microbial Science Institute (MSI)
Yale University
New Haven, CT 06520–8107, United States

V. C. Paingad, P. Kužel
Institute of Physics of the Czech Academy of Sciences
Na Slovance 2, Prague 18221, Czech Republic

E. J. Heilweil, T. J. Magnanelli
Nanoscale Spectroscopy Group
Nanoscale Device Characterization Division
NIST
Gaithersburg, MD 20899, USA

Table 1. Comparison of OPTP, TRMC and device techniques.

	OPTP	TRMC	Hall	solar cell
electrical contacts	possible	not allowed	required	required
results	sum mobility ^{a)} decay time		Mobility (doping)	
carrier kind	photo-excited carriers (electrons, holes, excitons, polaritons)		Dark majority carriers	all carriers
photoexcitation	Pulsed	pulsed	no	continuous
transport frequency	0.5–3 THz	8–12 GHz	DC	DC
transport direction	Lateral	lateral	lateral	vertical
transport distance	≈20 nm ^{b)}	≈200 nm ^{b)}	≈1 cm	≈500 nm
transient-window	100 fs – 2 ns	10 ns – 1 ms ^{c)}		
sensitivity	$\mu > 0.1 \text{ cm}^2 \text{ V}^{-1} \text{ s}^{-1}$	$\mu > 10^{-4} \text{ cm}^2 \text{ V}^{-1} \text{ s}^{-1}$		

^{a)}frequency-resolved version (Time-resolved terahertz spectroscopy) additionally yields the reduced effective mass, the scattering time, and an indication of carrier localization; ^{b)}Probed transport distance is proportional to the root of the charge carrier mobility, here for $30 \text{ cm}^2 \text{ V}^{-1} \text{ s}^{-1}$; ^{c)}time resolution of 0.5 ns can be realized by open-cell configuration at 30 GHz.

Halide perovskites represent a semiconductor class that has undergone enormous progress in their application as light-harvesting and emitting material. The corresponding solar cells have certified power conversion efficiencies of 25.5 %, outperforming $\text{Cu}_2(\text{In,Ga})(\text{S,Se})_2$ (CIGS) and CdTe thin-film technologies.^[1] The remaining losses in the fill factor and open circuit voltage have been attributed to limited charge transport and non-radiative recombination, respectively.^[2] In principle, OPTP and TRMC are ideal for probing these losses and numerous OPTP and TRMC studies have been conducted on lead-halide

perovskites so far.^[3,4] However, since for these measurements an electrical potential corresponding to solar cell operating conditions cannot be applied (due to the lack of contacts), the OPTP and TRMC measurement conditions must be translated to the thin film device. Such differences are summarized in **Table 1** and require several steps of interpretation and modeling, which have been handled differently by different research groups so far. Therefore, this publication seeks a consensus on the interpretation of TRMC and OPTP measurements and discusses the confidence of the results.

The first step is to characterize carrier trapping and exciton formation, as the corresponding quantum yields are crucial for assigning relevant lifetimes and electron and hole mobilities. Therefore, theoretical signatures of trap filling, exciton formation, and the excitonic Mott transition are discussed for the injection-dependent mobility and photoconductivity transients.

Second, a solar cell is operated under continuous 1 sun illumination while OPTP and TRMC are measured after pulsed excitation. Therefore, the injection dependence of the effective lifetime is measured and the value that corresponds to solar cell operation is determined. Modeling the occupation of the band states allows deriving the implied open-circuit voltage and the implied current-voltage characteristics without transport losses.

Third, OPTP (or TRMC) measures the mobilities of charge carriers in electric fields that alternate at THz (or GHz) frequencies, which must be translated to the DC-transport through the thin-film solar cells. However, previous publications do not agree on whether the transport is reduced by charge carrier localization or not. Here, we discuss the impact of transport barriers at grain boundaries on the frequency-dependence and underline differences between long-range and short-range DC-transport. Simulations of the JV-characteristics with the drift-diffusion modeling software SCAPS-1D reveal whether the OPTP-derived intra-grain mobilities account for the fill factor losses in the complete solar cell.

Fourth, the precision of our results is determined by an inter-laboratory comparison. The reviews of Savenije and Herz showed that the reported charge carrier mobilities for standard halide perovskites such as methylammonium lead iodide vary considerably from 1 to $600 \text{ cm}^2 \text{ V}^{-1} \text{ s}^{-1}$.^[3,4] Although similar mobility variations have been reported for conventional

J. A. Spies
Department of Chemistry and Energy Science Institute (ESI)
Yale University
New Haven, CT 06520–8107, United States
M. Schleuning, D. Friedrich, K. Schwarzburg
Institute for Solar Fuels
Helmholtz-Zentrum Berlin für Materialien und Energie GmbH
Hahn-Meitner-Platz 1 14109, Berlin, Germany
P. Dörflinger, V. Dyakonov
Chair of Experimental Physics 6
Faculty of Physics and Astronomy
Julius Maximilian University of Würzburg
97074, Würzburg, Germany
R. Katoh
Department of Chemical Biology and Applied Chemistry
College of Engineering
Nihon University
Fukushima 963–8642, Japan
M. J. Hong, J. G. Labram
School of Electrical Engineering and Computer Science
Oregon State University
Corvallis, OR 97331, USA
M. Monti, E. Butler-Caddle, J. Lloyd-Hughes
Department of Physics
University of Warwick
Gibbet Hill Road, Coventry CV4 7AL, United Kingdom
M. M. Taheri, J. B. Baxter
Department of Chemical and Biological Engineering
Drexel University
Philadelphia, PA 19104, United States
S. Luo, J. M. Cardon, S. Ardo
Department of Chemistry
Department of Chemical & Biomolecular Engineering
Department of Materials Science & Engineering
University of California Irvine
Irvine, CA 92697, United States

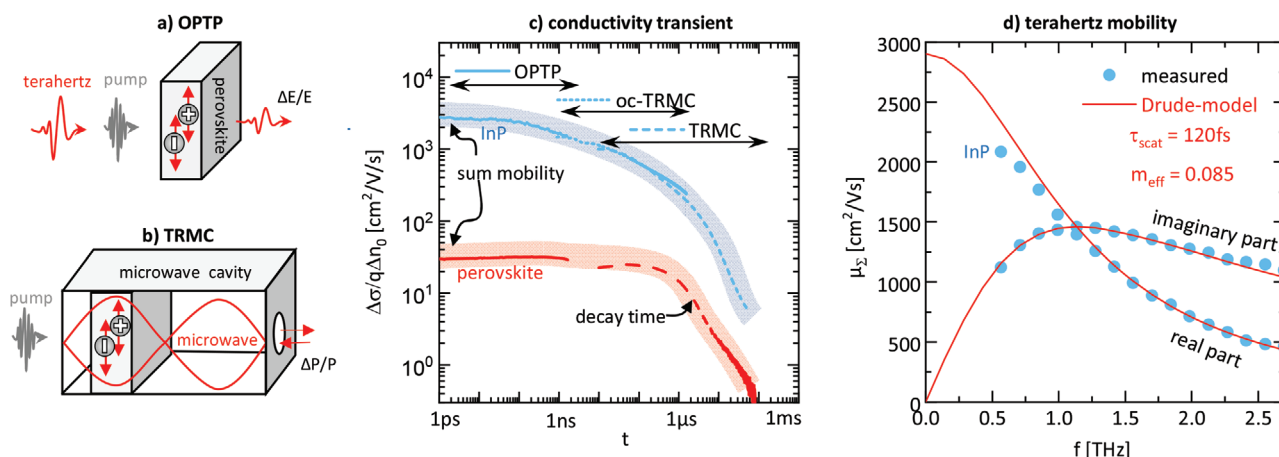


Figure 1. OPTP and TRMC in a nutshell: Illustration of a) optical-pump terahertz-probe measurements (OPTP) and b) time-resolved microwave conductivity measurements (TRMC). c) Photoconductivity transients measured on an InP-wafer and on a $\text{Cs}_{0.05}(\text{FA}_{0.83}\text{MA}_{0.17})_{0.95}\text{Pb}(\text{I}_{0.83}\text{Br}_{0.17})_3$ thin film. The time windows of OPTP and TRMC are bridged by open-cell TRMC (oc-TRMC). The mobility is estimated from the initial amplitude and the lifetime from the transient behavior. d) Time-resolved terahertz spectroscopy (TRTS) on InP—a frequency-resolved version of OPTP—yields the mobility spectra of the real and imaginary parts of the mobility. Fitting the carrier mobility in InP with the Drude-model yields an effective scattering time of 120 fs and a reduced relative effective mass of 0.085.

techniques, such as Hall measurements, concerns have arisen in the semiconductor community about “non-standard” mobility measurements like OPTP and TRMC.^[5] To characterize the measurement variations, we studied the charge carrier mobility in fifteen TRMC and OPTP laboratories and were thus able to statistically decouple the inter-laboratory variations from the intrinsic material properties. To this end, the participating laboratories received perovskite thin films with a nominal stoichiometry of $\text{Cs}_{0.05}(\text{FA}_{0.83}\text{MA}_{0.17})_{0.95}\text{Pb}(\text{I}_{0.83}\text{Br}_{0.17})_3$ on fused silica and for comparison wafers of single-crystalline InP. All halide perovskite samples were fabricated at the University of Potsdam under identical preparation conditions in one go, as described in the Note S1, Supporting Information. The preparation conditions used, have previously resulted in solar cells with more than 20% efficiency.^[6]

2. OPTP and TRMC in a Nutshell

The contactless nature of the measurement is a major advantage of OPTP and TRMC over more conventional techniques such as DC-conductivity and Hall-effect measurements, as it overcomes interface issues such as contact resistance, unintentional doping, and bandwidth limitations and allows to study bare films and even powders.^[7] OPTP in reflection mode is even more flexible as it allows probing interfaces between semiconducting materials and highly conductive substrates.^[8]

Both techniques have in common that they probe the formation and kinetics of photoexcited electrons, holes, and excitons by measuring photoconductivity transients, as well as mobilities. OPTP and TRMC are based on the same principles as illustrated in Figure 1a/b. Typical experimental setups are described in Notes S2 and S3, Supporting Information.^[9,10] Optical pump pulses photogenerate charge carriers in the (perovskite) sample. Depending on their mobilities, these carriers are accelerated laterally in an electric field of a terahertz probe pulse or by a standing microwave in a cavity, which alter-

nate at terahertz or gigahertz frequencies, respectively. The photogenerated carriers acquire an oscillating drift velocity, and thereby a part of the terahertz or microwave radiation is absorbed. The corresponding pump-induced change in transmitted terahertz electric field $\Delta E/E$ or in the reflected microwave power $\Delta P/P$ is measured and analyzed in a first step for the sheet photoconductivity $\Delta\sigma_s$ or photoconductance ΔG . For our samples, the so-called Thin-Film Approximation (1) can be used for the OPTP analysis and Equation (2) for the TRMC analysis, which contain the vacuum permittivity ϵ_0 , the speed of light c , and the refractive index of the substrate n_{sub} or the sensitivity factor K .^[12]

$$\Delta\sigma_s = \int_{x=0}^d \Delta\sigma dx = -\epsilon_0 c (1 + n_{\text{sub}}) \frac{\frac{\Delta E}{E}}{1 + \frac{\Delta E}{E}} \quad (1)$$

$$\Delta G = \Delta\sigma_s \frac{a}{b} = -\frac{1}{K} \frac{\Delta P}{P} \quad (2)$$

The obtained sheet photoconductivity $\Delta\sigma_s = \int \Delta\sigma dx$ is given by the depth integral of the pump-induced conductivity $\Delta\sigma$. The depth distribution of the photoconductivity (or of the carrier concentration) is irrelevant for the OPTP and TRMC measurements on thin films. Alternatively, the OPTP-community often uses the mean photoconductivity $\Delta\sigma = \Delta\sigma_s/d$, which assumes a homogeneous distribution of the carriers over the sample thickness d . The TRMC community uses the quantity (lateral) photoconductance ΔG , which has the same units as sheet conductivity but is scaled by the ratio of the sample length in the direction of the microwave field b and the sample length perpendicular to the microwave field a . To underline that OPTP and TRMC measure in principle the same quantity and to be independent of the sample dimensions we convert TRMC-derived photoconductance into sheet photoconductivity in this work.

The sheet photoconductivity is measured either by varying the delay between the optical pump pulse and the terahertz probe pulse or from the transient microwave power reflected from the sample in TRMC, resulting in complementary transients as shown for a perovskite thin film and an InP wafer in Figure 1c. A major difference between the two techniques is the accessible time window, which is typically 100 fs – 2 ns for OPTP and 10 ns – 1 ms for TRMC. Hence, OPTP can probe materials with relatively short charge carrier lifetimes such as early-stage emerging materials, CdTe and kesterites; whereas TRMC is suited for materials with longer lifetimes such as passivated Si or GaAs-wafers, Cd(Se,Te), and halide perovskites. However, the time window of OPTP has been previously increased to similar values as for TRMC by using a separate laser for terahertz generation and photoexcitation.^[13] The lower time resolution of the TRMC is due to the finite quality factor of the resonator: Using an open cell (oc) can improve the time resolution of the TRMC to below 1 ns, but at the expense of sensitivity. For example, cavity resonance lowers the time resolution but is also largely responsible for TRMC's better sensitivity for mobilities of $>0.0001 \text{ cm}^2 \text{ V}^{-1} \text{ s}^{-1}$ compared to $>0.1 \text{ cm}^2 \text{ V}^{-1} \text{ s}^{-1}$ for OPTP at injection levels of $\approx 10^{14}$ photons per pulse and cm^2 .

The sheet photoconductivity transients $\Delta\sigma_s$ shown in Figure 1c can be caused either by a decay in the electron-hole pair concentration Δn_s via recombination, or by a decay in the average mobility via transfer into a contact layer with lower mobility, or trapping, or exciton formation. For deriving a lifetime related to recombination, it is crucial to distinguish these processes, which will be discussed in the next section.

$$\Delta\sigma_s = e\Delta n_s\mu_\Sigma \text{ with } \mu_\Sigma = \Phi(\mu_e + \mu_h) \text{ and } \mu_{e/h} = (1 - \Phi_{\text{trap}})\mu_{\text{band}} \quad (3)$$

The sum mobility μ_Σ can be gained from Equation (3), if the initially induced sheet carrier concentration Δn_s is measured as elaborated in detail in the Note S4, Supporting Information. Therefore, the sheet photoconductivity transients are often divided by the elementary charge e and the initial induced sheet carrier concentration Δn_s as shown in Figure 1c, which allows reading the sum mobility from the initial amplitude of the transient. However, the mobility is not necessarily changing over time, which may be unintentionally suggested by this representation.

The sum mobility μ_Σ is twice the average mobility of all photo-generated species that are weighted by their concentrations. In most cases, it can be described in Equation (3) by the sum of the average electron mobility μ_e and of the average hole mobility μ_h , and by the fraction Φ of electron and hole pairs that are not bound as excitons, which is usually called free-carrier quantum yield. However, dissociated electron-holes pairs can also be trapped in defect states where they are usually immobile and not “free”. In such cases, the average electron mobility μ_e is reduced compared to the mobility in the conduction (or valence) band μ_{band} by the fraction Φ_{trap} of electrons that are trapped. The overall fraction of free photoexcited electrons is given by $\Phi_e = \Phi(1 - \Phi_{\text{trap}})$. Holes can be treated analogously with individual trapping fractions.

In terahertz spectroscopy, the mobility is usually obtained from measuring the full shape of the electric field of the

terahertz pulse at a fixed time after charge carrier photogeneration, which is detailed in Note S2, Supporting Information. Such measurements are called Time-Resolved Terahertz Spectroscopy (TRTS). This technique has the advantage, that a Fourier-transform reveals the real and imaginary part of the mobility as a function of the terahertz frequencies that constitute the terahertz pulse. Typical windows are $\approx 0.5\text{--}2.5 \text{ THz}$ for TRTS versus a single frequency of typically $\approx 9 \text{ GHz}$ for TRMC. For many single-crystalline materials, such as InP shown in Figure 1d, the frequency dependence follows the Drude-model, which allows to determine the reduced effective mass, the effective scattering time, and to extrapolate the DC-mobility of the charge carriers. The frequency dependence for halide-perovskites is more challenging to analyze and demands more advanced models as will be discussed in Section 5.

3. Exciton Formation and Trapping

The possible impact of trapping and exciton formation must be clarified to determine the mobility and the effective lifetime that are relevant for (photovoltaic) applications. Employing the above band-gap excitation light, charge carriers are generated with excess kinetic energy, which is more than 1 eV per electron-hole pair in the case of 3.1 eV pump photons and a 1.65 eV bandgap of the studied perovskite. Subsequent carrier cooling, trapping, exciton formation, and recombination are schematically depicted in Figure 2a.

3.1. Trapping Signature

Trapping signatures in the photoconductivity kinetics are modeled and shown in Figure 2b–d for the presence of a shallow electron trap and a deep recombination center. The modeled photoconductivity exhibits a fast decay due to the initial capture into the trap states. The recombination leads to the subsequent decrease with the effective lifetime $\tau_{\text{eff}} = \tau_{\text{SRH}} / (1 - \Phi_{\text{trap}})$, where the Shockley–Read–Hall lifetime τ_{SRH} is prolonged by the fraction of trapped carriers Φ_{trap} .^[14–16] For low carrier concentration this fraction increases during the initial capture to the value given by Equation (4). For large concentrations, the traps get filled, and the effective mobility increases towards the mobility in the band states, which is demonstrated in Figure 2e.

$$\Phi_{\text{trap}} \approx 1 - \frac{N_{c/v}}{N_t} \exp\left(-\frac{E_t}{k_B T}\right) \text{ for } n \ll N_t \quad (4)$$

In case of high defect concentrations, defect bands may be formed, in which carriers have rather small mobility, or the mobility may continuously fade out in band tails. However, the signatures of a reduced mobility, trap-filling, and thermal activation are maintained.

3.2. Exciton Signature

Since excitons carry no effective charge, their DC-mobility is zero. They can be polarized by THz radiation or excited

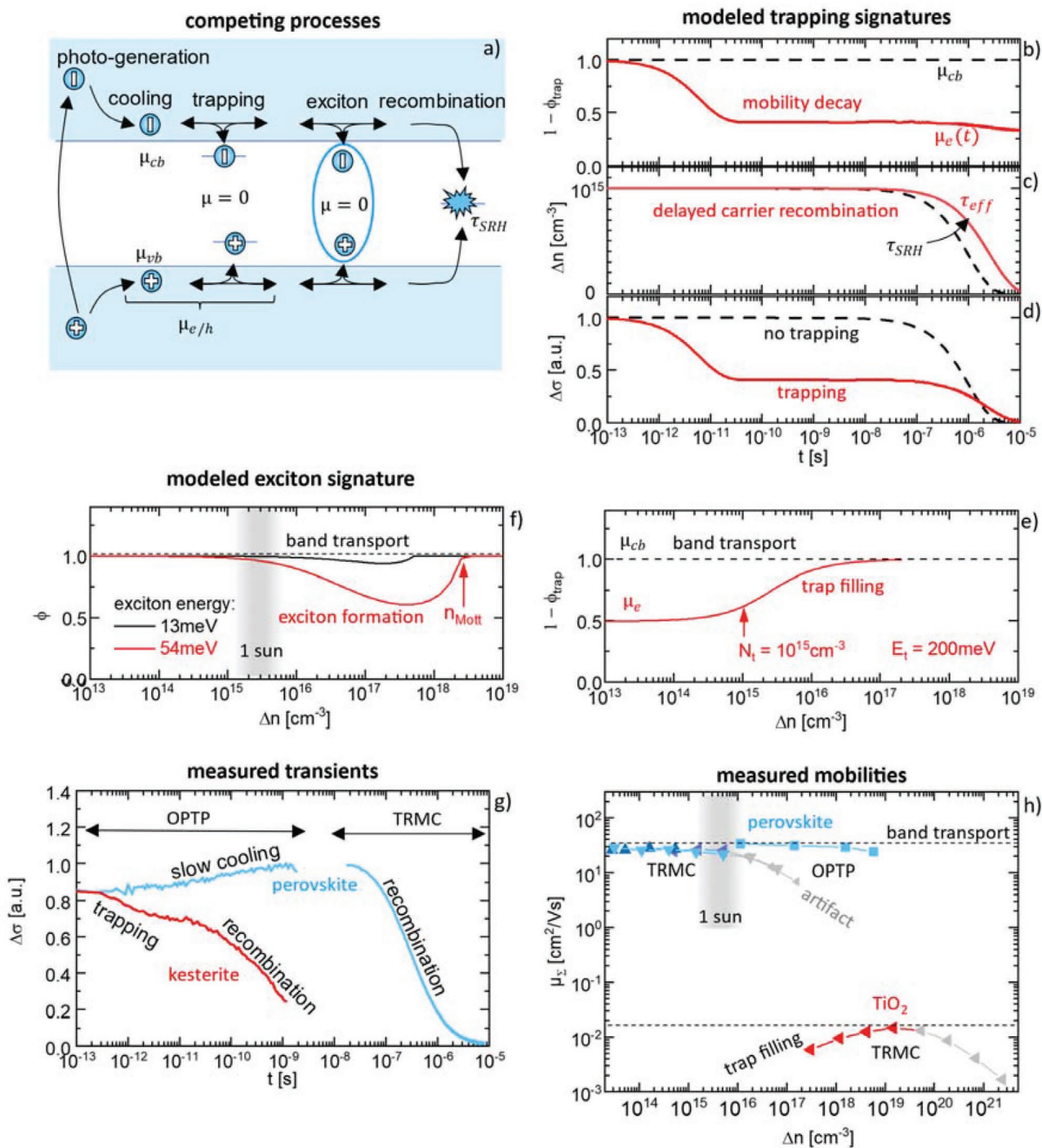


Figure 2. Probing exciton formation and charge carrier trapping. a) Illustration of competing charge carrier dynamics including cooling to the band-edge, trapping, exciton formation, and recombination. b–d) Signatures of trapping in the modeled transients of trapping fraction Φ_{trap} , carrier concentration Δn , and photoconductivity $\Delta\sigma$ for electron traps with a discrete energy level E_t of 200 meV, a trap concentration N_t of 10^{15} cm^{-3} , a trapping time of 10 ps, a Shockley–Read–Hall lifetime τ_{SRH} of 1 μs , and effective density of band states $N_{c/v}$ of $2.2 \times 10^{18} \text{ cm}^{-3}$. e) Effect of trap filling increases the quantum yield to unity. f) Effect of exciton formation, which typically reduces the quantum yield at intermediate carrier concentrations and excitons dissociate above the Mott transition concentration n_{Mott} . g) The photoconductivity transient of a kesterite thin film exhibits a fast decay due to trapping and a long decay due to recombination. The lead-halide perovskite sample exhibits no initial decay, which indicates the absence of trapping and exciton formation. h) The sum mobility of a TiO_2 thin film increases with injection level, which indicates trap-filling. No significant injection dependence is observed for the lead-halide perovskite sample, which indicates band transport without exciton formation.

into a higher state if their binding energy is close to the THz photon energy (4 meV at 1 THz). Such processes lead to Lorentz-oscillator-like features in the sum mobility spectra.^[17–19] However, excitonic features are usually negligible compared to the mobility of free charge carriers. Hence, the conversion of free electrons and holes into excitons reduces the photoconductivity and sum mobility, and can be described by the free-carrier quantum yield Φ in the Saha-Equation.^[20] Here, we use a modified version, which takes into account that exciton binding energies E_{ex} decrease, and excitons dissociate when the free carrier concentration approaches the Mott threshold (Note S5, Supporting Information).^[21] The injection dependence of the excitonic quantum yield is shown in Figure 2f, where the assumed exciton binding energies of 13 and 54 meV reflect the debated range for lead-halide perovskites.^[22] The modeling shows that even a rather unrealistically large E_{ex} of 54 meV does not lead to significant exciton formation at carrier concentrations of 10^{15} cm^{-3} , which corresponds to typical 1 sun illumination conditions for a halide perovskite solar cell. Hence excitons should not significantly affect the room temperature sum mobility and photoconductivity transients in lead-halide perovskites. Previous works on lead halide perovskites used the original Saha Equation, which does not take into consideration the Mott transition.^[23–25] While it yields similar results as the modified Saha equation at 1 sun conditions, it can significantly underestimate the free carrier quantum yield at high injection levels that are common for OPTP measurements, as shown in Figure S5, Supporting Information.^[25] Subsequently this would lead to an overestimation of the OPTP-derived sum of electron mobility and hole mobility.

3.3. Experimental Evidence

The impact of excitons and traps can be probed experimentally by TRMC and OPTP. To this end, the measured injection-dependence, time-dependence (and temperature-dependence) of the mobility are compared to the characteristic behavior of excitons and trapping that were modeled in Figure 2b–f.

A typical fast photoconductivity decay by trapping and a longer component by delayed recombination are observed for example by OPTP for a kesterite ($\text{Cu}_2\text{ZnSnSe}_4$) thin film in Figure 2g. In contrast, the photoconductivity of the perovskite thin-film shows a modest increase in photoconductivity, which can be explained by slow cooling of photogenerated charge carriers.^[26] Carriers relax from high energetic states with rather low mobility to the band edges with higher mobility. No further relaxation into traps or excitons seems to occur. Hence, the decay observed in the perovskite sample by TRMC can be attributed to recombination that is not affected by exciton formation nor prolonged by de-trapping.

Due to its limited time-resolution, TRMC usually measures the sum mobility after the initial capture into shallow trap states. For defect-rich materials such as TiO_2 , the TRMC-derived sum mobility is known to exhibit the signature of trap-filling in the injection dependence, which is shown in Figure 2h.^[27,28] However, the measured sum mobility of the perovskite sample is constant over a large range of induced carrier concentrations from 10^{13} to 10^{18} cm^{-3} . Such behavior indicates that either traps

are not occupied due to thermal activation into the bands or that the density of trap states is below 10^{13} cm^{-3} .

The observed small decrease of the OPTP-mobility for carrier concentrations above 10^{18} cm^{-3} may be assigned to a degenerate filling of the band states as the effective density of the band states is reached. Electron-hole scattering may also contribute. The decrease of the TRMC-derived mobility for induced carrier concentrations above $\approx 10^{16} \text{ cm}^{-3}$ is related to the recombination of charge carriers within the time resolution.^[29] Therefore, it can be treated as an artifact (see Figure 2h, grey symbols), which is not apparent in the OPTP-derived measurements.

We conclude that at 1 sun equivalent illumination, mobilities and lifetimes are not affected by exciton formation for exciton binding energies below $2k_{\text{B}}T$ ($\approx 50 \text{ meV}$ at room temperature), which is generally the case for lead-halide perovskites except for very high Br or Cl contents.^[22] Further, lead-halide perovskites can have such high quality that shallow traps become irrelevant for mobility and lifetime under 1 sun equivalent illumination. Then, the sum mobility is the sum of conduction band and valence band mobilities, that is, there is no defect nor band-tail transport.

4. Charge Carrier Recombination

Carrier lifetimes characterize the strength of charge carrier recombination and are directly related to the quasi-Fermi level splitting and thus the maximum open-circuit voltage (V_{OC}) that a material can support in a device.^[30,31] This implied voltage could be realized if the probed neat material is contacted with ideal transport layers. Therefore, carrier lifetimes are widely used as a metric by material scientists to guide the development of photovoltaic materials. However, a review of the literature shows that derived lifetimes from OPTP and TRMC measurements can vary by orders of magnitude, even on the same sample. Here it will be shown that these variations are mostly a consequence of the different injection levels and accessible time windows. OPTP and TRMC are complementary and together can probe photoconductivity transients in an extremely large time window from femtoseconds to milliseconds and for injection levels from 10^{13} to 10^{19} cm^{-3} as shown in Figure 3a. After identifying the relevant injection level and lifetime for photovoltaic application, the implied V_{OC} and current-voltage curve can be determined.

4.1. The Relevant Lifetime

For the same perovskite thin film, injection-dependent transients were measured by OPTP, TRMC, open-cell TRMC (oc-TRMC), and time-resolved photoluminescence (TRPL) and are shown in Figure 3a and Figure S6, Supporting Information. A rather complex modeling of such transients can yield a detailed understanding of the underlying kinetics, such as revealing the dominant recombination process, defect densities, doping concentration, and charge transfer rates to contact layers.^[3] However, here a relatively simple approach is taken that allows estimating the potential JV-curve of the finished solar cell independently of the details of the recombination process. To this

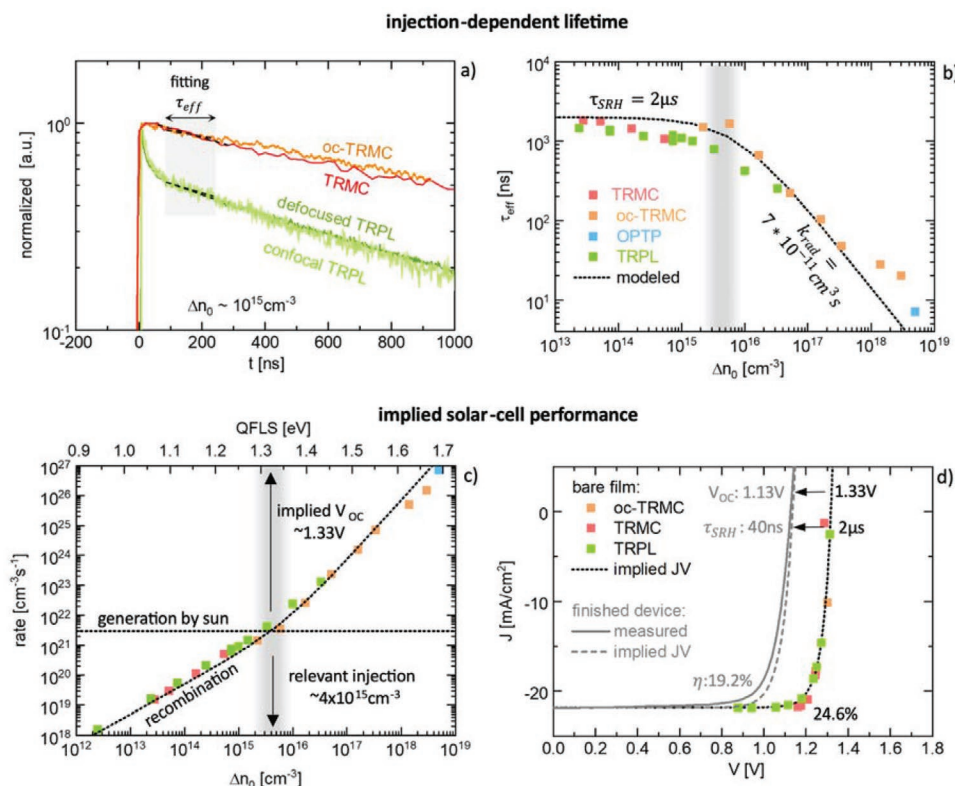


Figure 3. The relevant lifetime and the implied V_{oc} a) Normalized photoconductivity measured on the perovskite thin film by a TRMC at 9 GHz and an open-cell (oc-) TRMC at 30 GHz, as well as transient photoluminescence measured at initial photogenerated carrier concentration of $\approx 10^{15} \text{ cm}^{-3}$ assuming a homogeneous carrier distribution throughout the perovskite layer thickness. The initial TRPL decay is not related to recombination and the fitting region for the effective lifetime is indicated. b) Effective lifetime as a function of the generated carrier concentration is modeled with a constant Shockley-Read-Hall lifetime τ_{SRH} and a radiative recombination coefficient k_{rad} . The gray area indicates 1 sun condition. c) The generation rate under continuous 1 sun illumination and the recombination rates at different carrier concentrations that are derived from the measured lifetimes. The balance of recombination and generation defines the relevant carrier concentration under 1 sun illumination and the implied open-circuit voltage (V_{oc}). d) Implied current-voltage (JV) curve with 24.6% efficiency that the bare perovskite thin-film could realize in an ideal finished solar cell without transport or contact losses. The measured JV-curve exhibits much lower V_{oc} , which corresponds to a reduced lifetime of 40 ns, likely due to additional recombination at the C_{60} interface.

end, the initial decay of TRMC and OPTP transients are modeled with a single exponential decay $\exp(-t/\tau_{eff})$, which quantifies the strength of the recombination at the initially induced carrier concentration with an effective lifetime τ_{eff} . The TRPL transients exhibit an additional decay component in the first ≈ 20 ns, which is not apparent in the TRMC or OPTP transients. Therefore, this decay cannot be connected to recombination and potentially is caused by charge carrier redistribution. Hence, the effective TRPL lifetime is fitted to the second decay component, as indicated by the gray area in Figure 3a.

The determined effective lifetimes τ_{eff} depends on the initially induced carrier concentrations Δn_0 as shown in Figure 3b. Indeed, the values retrieved by TRPL, TRMC, and oc-TRMC at a specific intensity agree relatively well with each other, which further supports the attribution of the corresponding decays to recombination.

Each technique has unique features: A limitation of TRMC is that at high injection, the lifetime drops below the time-resolution and cannot be resolved.^[29] The main limitation of OPTP is the time window of up to ≈ 2 ns for standard setups, which allows to only detect lifetimes up to ≈ 10 ns, and a possible divergence of the pump beam while scanning the delay line

can lead to artificial transients.^[32] A pitfall for TRPL analysis is that the decay time at high injection is half of the charge carrier lifetime since the photoluminescence emission in this case, is proportional to $\approx \Delta n^2$, which may explain partially the slightly lower TRPL-derived decay times in Figure 3b. Further variations were observed between the transients measured by participating TRMC laboratories on their individual samples. While the material was fabricated in a single batch, shipping, storing, and handling could result in a stronger sample-to-sample variation than anticipated. Recombination and lifetimes are much more sensitive to defect concentrations in the individual samples compared to the charge carrier mobility.

A further uncertainty lies in the estimation of the photo-generated carrier concentration Δn_0 . For excitation with a wavelength of 400 nm, as common for OPTP measurements, the carrier concentration at the surface is ≈ 10 times larger than the homogeneous distribution throughout the entire film thickness d of ≈ 500 nm, which is reached after the time $\tau_D > d^2/D$ of ≈ 6 ns. Hence, the OPTP time window of ≈ 2 ns probes rather the initial carrier distribution, whereas the TRMCs time resolution of ≈ 10 ns probes the homogeneous one. Additionally, surface recombination can lead to faster initial recombination that

becomes less dominant when carriers have diffused throughout the layer thickness.^[32] In such cases, fitting the initial decay does not represent the charge carrier lifetime in the steady-state, which is relevant for PV applications. Instead, to predict PV performance, the longtime component—after the diffusion time τ_D —should be used. In our case, the initial decay time of $\approx 1 \mu\text{s}$ is much longer than the diffusion time. Therefore, potential surface recombination cannot be distinguished from bulk recombination and no fast initial component can be observed, which leads to simple mono-exponential decays at low injection levels.

An effective lifetime τ_{eff} can contain contributions from Shockley–Read–Hall recombination via deep trap states, from radiative recombination, and from Auger recombination. In general, the effective lifetime depends on the carrier concentration Δn . The Shockley–Read–Hall lifetime can to first-order be approximated as injection-independent, but the radiative recombination coefficient k_{rad} and the Auger recombination coefficient k_{Auger} lead to a decreasing lifetime with increasing carrier concentration.^[33]

$$R = \frac{d\Delta n}{dt} = -\frac{1}{\tau_{\text{eff}}} \Delta n \text{ with } \frac{1}{\tau_{\text{eff}}} = \Phi_{\text{trap}} \left(\frac{1}{\tau_{\text{SRH}}} + k_{\text{rad}} \Delta n + k_{\text{Auger}} \Delta n^2 \right) \quad (5)$$

Such a decrease is measured for the perovskite sample and is modeled in Figure 3b by a transition from an effective Shockley–Read–Hall lifetime of $\tau_{\text{SRH}} \approx 2 \mu\text{s}$ at low injection to radiative recombination with an (external) radiative coefficient of $k_{\text{rad}} = 5 \times 10^{-10} \text{ cm}^3 \text{ s}^{-1}$. This coefficient lies in the relatively broad range of literature values for MAPbI₃ from 1.1×10^{-10} to $8 \times 10^{-9} \text{ cm}^3 \text{ s}^{-1}$.^[33–37]

4.2. The Implied JV-Curve

The implied open-circuit voltage and the relevant lifetime under 1 sun illumination can be determined directly from the measured effective lifetimes and the corresponding recombination rates $R = -\Delta n/\tau_{\text{eff}}$. The generation rate G by 1 sun illumination is $\approx 3 \times 10^{21} \text{ carriers} \times \text{s}^{-1} \text{ cm}^{-3}$ for the terrestrial solar spectrum ϕ_{sun} (AM1.5G in this work), for an absorptance a , which can be approximated with a step-like onset at the bandgap energy $E_G = 1.65 \text{ eV}$, and for a film thickness d of 500 nm. Further, a reflectance r of 9 % is assumed. Such continuous illumination of a bare material or a solar cell in open circuit conditions builds up a carrier concentration of $1.5 \times 10^{15} \text{ cm}^{-3}$ until the charge carrier generation rate G is balanced by the recombination rate $R = G$, which is shown in Figure 3b. The lifetime of $\approx 1 \mu\text{s}$ at this carrier concentration is the relevant one for photovoltaic application.

$$G = (1-r) \frac{\int a \phi_{\text{sun}} dE}{d} \quad (6)$$

The carrier concentration (at the 1 sun conditions) implies a splitting of the quasi-Fermi levels of electrons and holes ΔE_F . The corresponding implied V_{OC} is given by the bandgap E_G , the effective density of states of the conduction N_C and valence band N_V , and the electron concentration in the conduction

band n_c and the hole concentration in the valence band p_v . The effective densities of states are determined by their effective masses m_e and m_h . The carrier concentrations in the bands are determined by the doping n_0 (or p_0), the concentration of photogenerated carriers Δn and Δp , and by the fraction of carriers that relax into trap states Φ_{trap} . The measured effective lifetimes imply a V_{OC} of $\approx 1.31 \text{ V}$ for an intrinsic perovskite material ($n_0 = p_0 = 0$).

$$V_{\text{implied}} \approx \frac{\Delta E_F}{q} = \frac{E_G}{q} + \frac{k_B T}{q} \ln \left(\frac{n_c}{N_C} \frac{p_v}{N_V} \right) \text{ with } n_c = (1 - \Phi_{\text{trap}}) (\Delta n + n_0) \quad (7)$$

$$N_{C/V} = 2 \left(\frac{2\pi m_{e/h}^* k_B T}{h^2} \right)^{3/2} \quad (8)$$

A pitfall in this context is the presence of trapping: Ideal shallow traps (trapped carriers are reemitted into the band states before they recombine) do not affect the V_{OC} . The trapping quantum yield increases the lifetime and subsequently the total carrier concentration, but only the carriers in the band states contribute to the V_{OC} . In consequence, the trapping quantum yield in Equation (5) for the lifetime and in Equation (7) for the V_{OC} cancel out. However, for the interpretation of a measured lifetime, it is important to know if it is artificially increased by trapping and how it relates to the V_{OC} .

$$J = e [G_{\text{sun}} - R(V_{\text{implied}})] d \quad (9)$$

Beyond the implied V_{OC} , the full implied JV-curve can be calculated by the detailed balance of recombination and generation using Equation (9), which is inspired by the analysis of suns- V_{OC} or suns-PL measurements.^[38] The difference of charge carrier generation and recombination is supplied or extracted by an external current density J . The JV-curve implied by the measured effective lifetimes is shown in Figure 3d. Assuming an intrinsic perovskite layer, the lifetimes of the bare absorber imply a possible efficiency of 24.6 % for the finished solar cell. For frequently reported doping of $\approx 10^{15} \text{ cm}^{-3}$,^[33] the implied efficiency increases to 25.6 %, which is mostly a result of an increasing fill-factor from 0.850 to 0.883.

The complete solar cell exhibits a JV-curve with a much lower V_{OC} . Such differences between the implied V_{OC} of the bare material and the device, were previously assigned to additional recombination at the interface to the LiF/C₆₀ electron transport layer, which reduced the TRPL decay time to $\approx 20 \text{ ns}$.^[6] Additionally, hole transport layers (HTLs) such as PTAA and spiro-OMeTAD can induce recombination.^[30] In our case, the effective lifetime must be reduced from $2 \mu\text{s}$ to 40 ns to reproduce the measured V_{OC} of 1.13 V, which translates for an intrinsic perovskite into a TRPL decay time of 20 ns.

However, the implied JV-curve with the lower assumed lifetime still overestimates the fill factor of the finished solar cell (grey lines in Figure 3d). Such fill factor losses are usually assigned to transport losses as the implied JV-curves assume infinite charge carrier mobilities. The impact of the finite mobilities measured by TRMC and OPTP will be discussed at the end of the next section.

5. Modeling Device Transport from Gigahertz and Terahertz Mobilities

TRMC and OPTP measurements yield mobilities for charge carriers oscillating at GHz and THz frequencies. To characterize DC-device performance, the effective mobility relevant for direct transport through the thin film device must be estimated. To this end, the frequency-dependence retrieved from TRTS can be modeled, which additionally can reveal the nature of charge carrier transport and its limitations.^[9,11] Here, we will focus on transport in band states, as the previous section ruled out trapping into defect states or band tails for halide perovskites. However, charge carrier localization may still occur due to grain boundaries in polycrystalline thin films, which is debated for perovskites. Hence, using the modified Drude–Smith model we estimate for which domain sizes TRMC and TRTS yield inter-domain or intra-domain mobilities.^[39] The TRTS derived intra-grain mobilities are used to model the maximal JV-curve of the solar cell and the respective fill factor losses of the measured JV-curve are reproduced by a possible combination of insufficient transport in the contact layer and at grain boundaries.

5.1. Free Carrier Transport

A relatively simple interpretation of frequency-dependent mobilities can be given in the case of the InP wafer that was shown in Figure 1d. Exciton formation and trapping can be excluded due to the low exciton binding energy and the low defect density in such single-crystalline wafers. The real part of the measured mobility decreases with frequency, and the imaginary part is always positive, which are signatures of free charge carrier transport in band states. Such free transport of electrons and holes at the edges of conduction and valence band can be described by the Drude-model in Equation (10) with an effective mass m^* and an average scattering time τ_{scat} .

$$\mu_D(\omega) = \frac{e\tau_{\text{scat}}}{m^*} \frac{1}{1 - i\omega\tau_{\text{scat}}} \quad (10)$$

In principle, electron and hole transport should be modeled separately. However, it is common to assume equal scattering times for electrons and holes, as otherwise the modeling of the TRTS derived sum mobility is overparameterized. Under this assumption, a common scattering time of 120 fs and a reduced effective mass $1/m_r^* = 1/m_e^* + 1/m_h^*$ of 0.085 are retrieved from fitting the measured sum mobility spectrum, which is close to the literature values of ≈ 0.07 .^[40] Additionally, a DC value of $2900 \text{ cm}^2 \text{ V}^{-1} \text{ s}^{-1}$ for the sum of electron mobility and hole mobility is gained. Taking advantage of a previous density functional theory (DFT) calculation of the ratio of the effective masses of holes and electrons of 7.5 allows separating an individual electron DC-mobility of $2470 \text{ cm}^2 \text{ V}^{-1} \text{ s}^{-1}$ and a hole DC-mobility of $330 \text{ cm}^2 \text{ V}^{-1} \text{ s}^{-1}$.^[41] These DC-values characterize the DC-transport through a wafer-based potential solar cell and are close to previously reported Hall-derived electron mobilities of $\approx 2500 \text{ cm}^2 \text{ V}^{-1} \text{ s}^{-1}$ and hole mobilities of $\approx 200 \text{ cm}^2 \text{ V}^{-1} \text{ s}^{-1}$.^[42]

However, we note that an error in the free carrier quantum yield will result in equivalent errors in the retrieved effective

mass and the DC-mobilities of electrons and holes. In principle, the presence of excitons can be investigated by fitting the TRTS-derived photoconductivity spectra with $\Delta\sigma_s(\omega) = e\Delta n_s\Phi[\mu_e(\omega) + \mu_h(\omega)]$, which yields the free-carrier quantum yield as a free parameter.^[18,19] However, this approach relies heavily on assuming the correct transport model for the electron mobility $\mu_e(\omega)$ and hole mobility $\mu_h(\omega)$, and requires a known reduced effective mass (or a plasma frequency). In practice, the transport model (free or partially localized) is debated for perovskites as will be discussed later and this approach can result in rather unrealistic small quantum yields and overestimated electron and hole mobilities.^[43] Additionally, the TRTS-derived frequency dependence can be obscured by an insufficient overlap of terahertz and pump beams. This may lead to an artificial decrease of the measured mobility at lower frequencies, which is shown in Figure S12, Supporting Information, and may be misinterpreted as a sign of localized transport.

5.2. Phonon Features

The frequency-dependent mobility of the halide perovskite thin-film shown in Figure 4a does not convey such a clear trend as observed for InP. It is rather flat and exhibits artifacts from phonon modes, which complicates the analysis.

The phonon features occur at ≈ 1 and ≈ 1.8 THz and are not connected to the transport of photogenerated charge carriers. Instead, they originate from a photo-induced change in the phonon modes and their absorption of terahertz radiation.^[23] The terahertz absorption by phonon modes can also be seen in the permittivity shown in Figure 4b, which was adopted from.^[44] Several explanations were proposed for such phonon features in the sum mobility spectrum. In our case, this effect does not originate from a breakdown of the thin-film approximation in the OPTP analysis as reported by La-o-Vorakiat et al.,^[45] but could be explained by either coupling of the phonons to the induced carriers (polaron formation), or by phonon (lattice) heating or by screening the phonons with the induced free charge carriers.^[23,46] Despite the unclear mechanism, recent phenomenological fitting of the phonon features indicates that more than 90 % of the measured mobility amplitude can be attributed to electronic charge carrier transport and less than 10 % to the phonon artifacts.^[47] Still, the relatively weak frequency-dependence at terahertz frequencies is obscured, which complicates its modeling. For TRMC it was shown that the rotational modes in halide perovskites at 9 GHz cause no modulations of the TRMC-derived mobility.^[48,49] However, for materials with lower electronic mobility, such as perovskite quantum dots, such phonon features may dominate over the electronic sum mobility, and reporting the frequency spectrum is essential. Additionally, transitions between excitonic states or between quantum confined states can result in similar oscillator-like features, that should not be attributed to electronic transport.^[17]

5.3. Ultra-Frequent Scattering in Perovskites

Apart from the phonon features, the overall frequency-dependence is rather flat, with an imaginary mobility close to

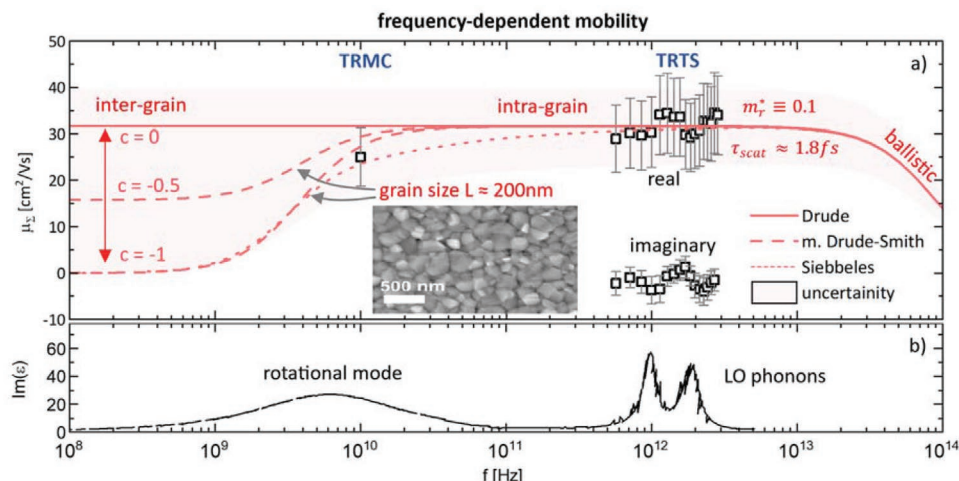


Figure 4. Modeling mobilities at THz and GHz frequencies. a) Spectrum of GHz and THz mobilities measured by TRMC and TRTS on the perovskite thin-film are described by several models for which the reduced effective mass is set to a literature value of 0.1 electron masses. The fitting results in a scattering time of 1.8 fs and intra-grain mobility of $32 \text{ cm}^2 \text{ V}^{-1} \text{ s}^{-1}$. The slightly lower TRMC mobility can be described by the modified Drude–Smith model or by the Siebbeles model with (partial) localization in grains with a size of $L = 200 \text{ nm}$ that is determined from the scanning electron microscope (SEM) image. Still, the uncertainty of the measured mobilities allows the localization parameter c to be varied from 0 for free transport through the grain boundaries to -1 for total localization of the carrier within the grains. b) The phonon modes seen in the permittivity ϵ (data adopted from [44]) cause artifacts in the OPTP-derived sum mobility at ≈ 1 and $\approx 1.8 \text{ THz}$.

zero, which implies extraordinarily short scattering times but opposes an independent determination of scattering time and reduced effective mass. When the transport frequency is larger than the overall scattering rate $1/\tau$, then ballistic transport occurs for which the mobility decreases and is exclusively determined by the effective mass. Such a decrease starts (90% of the initial value) approximately at a frequency of $f_{90\%} \approx 0.05/\tau$ and is therefore well-resolved in the typical TRTS range between 0.5 and 3 THz for InP with a scattering time of 120 fs. However, for the perovskite thin-film, no such decrease is observed. Therefore, here the reduced effective mass is fixed to a value of ≈ 0.14 , which corresponds to equal density of states effective masses of ≈ 0.2 that are reported for electrons and holes in lead-halide perovskites,^[33,50] and an increase by polaronic drag with a reported Fröhlich coupling constant of 1.72 to $m_p = m(1 + \alpha/6)$.^[51,52] With this mass, the modeling yields a scattering time of 1.8 fs, which is close to a previous study with wide-range OPTP that observed the mobility decay above 10 THz and retrieved 4 fs.^[53] Such extraordinary frequent scattering in perovskites has been attributed to longitudinal optical phonon scattering and a combination of lower phonon energies and large polarizability (dielectric constant).^[54]

Below the scattering rate $1/\tau$ (and above the localization frequency $1/2\tau'$), the (sum) mobility approaches the intra-grain DC-value $\mu_0 = q\tau/m_r$, which is $\approx 32 \text{ cm}^2 \text{ V}^{-1} \text{ s}^{-1}$ for the perovskite film. This lower mobility of the perovskite in comparison to InP is mostly caused by shorter scattering time and to a minor degree by a larger reduced mass. The similar effective masses of electrons and holes in halide perovskites suggest also similar electron and hole mobilities of $\approx 16 \text{ cm}^2 \text{ V}^{-1} \text{ s}^{-1}$. However, there is no direct evidence from TRMC or TRTS measurements themselves, and trapping, localization, and scattering may affect electrons and holes differently, which can lead to different effective electron and hole mobilities.

5.4. Microscopic Carrier Localization

The charge carrier mobility at lower frequencies can be further reduced by localization of carriers between transport barriers that are separated by a distance L , as modeled in Figure 4a by the modified Drude–Smith (Equations (11) and (12)) and by the Siebbeles model for total localization (Equation S7, Supporting Information).^[39,55] The characteristic negative imaginary part is shown in Figure S7, Supporting Information. In addition to the Siebbeles model, the modified Drude–Smith model can phenomenologically describe long-range transport through the barriers if a c -parameter is introduced similarly as in the original Drude–Smith model.^[56] This parameter may vary from $c = 0$ (Drude model) to $c = -1$ for full localization of carriers, leading to a Lorentz oscillator-like frequency-dependence. The interaction with the barriers shortens the effective scattering time τ'_{scat} in the Drude factor μ_D compared to the usual bulk scattering time τ_{scat} . The time τ' can be understood as the time to diffuse from one barrier to the other. The modified Drude–Smith model includes the Drude model for $c = 0$, the original Drude–Smith model for $\tau'_{\text{scat}} = \tau''$, and reproduces closely the Siebbeles model for $c = -1$ as can be seen in Figure 4a.

$$\mu_{\text{DS}} = \mu_D(\tau'_{\text{scat}}) \left(1 + \frac{c}{1 - i\omega\tau''} \right) \quad (11)$$

$$\frac{1}{\tau'_{\text{scat}}} = \frac{1}{\tau_{\text{scat}}} + 2\sqrt{\frac{k_B T}{m_{\text{eff}}}} \frac{1}{L} \quad \text{and} \quad \tau'' = \frac{m_{\text{eff}} L^2}{12k_B T \tau} \quad (12)$$

Whether the measured TRMC and OPTP mobilities at GHz and THz frequencies are reduced compared to the intra-grain value depends on the domain size L . The probed polycrystalline

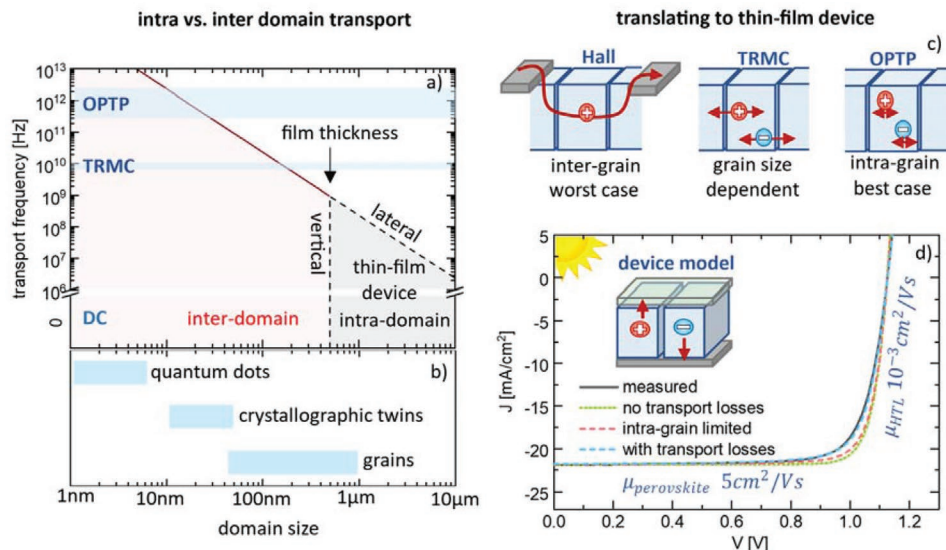


Figure 5. Modeling thin film devices from TRMC and OTP mobilities. a) For a given domain size, inter-domain transport is only relevant below a certain transport frequency which is given by Equation (13). Here for an intra-grain mobility of $15 \text{ cm}^2 \text{ V}^{-1} \text{ s}^{-1}$. If domains are larger than the film thicknesses, the vertical transport corresponds to intra-grain transport. b) Typical domain sizes in halide perovskites. c) Illustration of the translation of OTP and TRMC measurements to transport in a thin-film solar cell. d) Current-voltage curves of a solar cell modeled by SCAPS. The measured JV-curve is modeled by a possible grain-boundary limited effective mobility of $5 \text{ cm}^2 \text{ V}^{-1} \text{ s}^{-1}$. The OTP-derived intra-grain mobility of $15 \text{ cm}^2 \text{ V}^{-1} \text{ s}^{-1}$ allows larger fill factors.

perovskite thin film was imaged using SEM (inset of Figure 4a), from which a mean grain size of $L \approx 200 \text{ nm}$ was determined. For this size and an intra-grain mobility of $15 \text{ cm}^2 \text{ V}^{-1} \text{ s}^{-1}$, the mobilities at frequencies above $\approx 12 \text{ GHz}$ and in particular the OTP-derived mobilities at $\approx 1 \text{ THz}$ correspond to intra-grain transport. In contrast, TRMC-derived mobility at $\approx 9 \text{ GHz}$ can be reduced by such grain sizes. Despite the inter-laboratory variations, the median of the TRMC-derived mobilities in Figure 4a is indeed smaller, which may indicate the presence of transport barriers at grain boundaries in the probed perovskite thin film. Such interpretation is in line with previous TRMC-measurements at 9, 15, and 22 GHz on other perovskite thin films that showed an increasing mobility with frequency and a slightly negative imaginary component.^[57] Still, for our samples, unambiguous modeling is not possible as the full range of localization parameters from $c_1 = -1$ for total backscattering at these boundaries to $c_1 = 0$ for permeable grain boundaries is within the experimental confidence interval. Due to these uncertainties, we recommend regarding the measured mobilities at THz or GHz frequencies instead of modeled (long-range) DC-values when comparing mobilities published in different studies. This ambiguity in modeling is also reflected in literature, where OTP-derived mobilities of lead halide perovskites were described by the Drude model for free carriers,^[23,53,58] and by the Drude–Smith model for partial localization.^[43] TRMC-derived mobilities have been described by the Siebels model for total localization.^[55]

However, the original Drude–Smith model implicitly assumes $\tau'_{\text{scat}} = \tau''$, which implies that interacting with the domain walls is more frequent than bulk scattering and restricts its application to materials with extremely small domain sizes. Also, the measured mobilities could only be reproduced in Figure S7, Supporting Information, by the Drude–Smith model with a reduced relative effective mass of 1.7 (or low free-carrier

quantum yields), which conflicts with most of the literature values and therefore we excluded this model here.

To estimate if a known domain size can affect the mobility of a specific frequency, a localization frequency f'' can be defined in Equation (13), at which the mobility is reduced by total DC-localization ($c = -1$) to 90 % of the intra-grain value. This demarcation frequency is shown as the red line in Figure 5a for different domain sizes and an intra-grain mobility of $15 \text{ cm}^2 \text{ V}^{-1} \text{ s}^{-1}$.

$$f'' \approx \frac{1}{2\tau''} = 6 \frac{k_B T}{q} \mu_0 \frac{1}{L^2} \quad (13)$$

If the terahertz mobility shows signs of localization (negative imaginary part, real part increasing with frequency), which is not the case for our sample but was reported for other perovskite thin films,^[43] then the localization must occur within a domain smaller than 20 nm. Such small domains, for which OTP probes inter-domain transport, might be twin domains within grains,^[59] potential fluctuations due to dynamic disorder,^[60] or films of quantum dots. Previously, localization on length scales below the grain sizes was observed in kesterites and was attributed to band edge fluctuations due to local composition variations.^[61] The TRMC-derived mobility can be already reduced by grain sizes of $< 200 \text{ nm}$ and therefore can be very sensitive to the typical grain sizes of perovskite thin films.^[62] This finding contrasts with a recent study explaining a reduced THz mobility in a polycrystalline perovskite thin film by 100 nm sized grains.^[63] A possible explanation for this discrepancy is that the Mayadas and Shatzkes model used by Xia et al. describes DC-mobilities.^[64]

The so far discussed models, and the distinction between intra-domain and inter-domain transport, assume an infinitely extended material with sub-domains. However, in a thin film

device, the currents usually flow vertically through a film thickness of typically ≈ 500 nm for perovskite materials. Domain sizes larger than the film thickness can limit lateral transport but will not affect vertical transport. In such a case, the intra-grain mobility and possible barriers at interfaces with contact materials govern charge transport through the thin film, as illustrated in Figure 5a. Hence, long-range DC-mobilities as derived by the Drude, Drude–Smith, and Siebbeles models are not always relevant for the transport in the thin film device. Such inter-grain mobilities can be accessed by Hall measurements, which are performed over several mm, and are an estimate for the worst-case scenario for the transport in a solar cell. In contrast, the OPTP-derived intra-grain mobilities are an estimate for the best-case scenario for the transport in a solar cell, when grains extend from front to back or when the grain boundaries do not oppose transport. Such difference between Hall-derived inter-grain transport and TRTS-derived intra-grain transport has been reported for other thin-film materials.^[61]

5.5. Transport Losses in JV-Curves

In the following, we would like to clarify if the OPTP-derived intra-grain mobility causes transport losses in the finished device and is responsible for fill factor losses. To this end, JV-curves are modeled by the drift-diffusion simulation software SCAPS-1D 3.308 with parameters given in Note S8, Supporting Information.^[65] The JV-curve retrieved without transport losses (mobilities in all layers set to $1000 \text{ cm}^2 \text{ V}^{-1} \text{ s}^{-1}$) is shown in Figure 5c and agrees relatively well with the detailed balance analysis of the previous Section III (Figure S8, Supporting Information): The J_{sc} of 21.9 mAcm^{-2} is given by the absorbed sunlight and the V_{OC} of 1.126 V is reproduced for an effective bulk lifetime of 30 ns , which is the sum of electron capture time and hole capture time. Interestingly, the fill factor that was simulated by SCAPS of 0.841 is larger than the one retrieved by the detailed balance analysis of 0.820 . Such larger fill factors are possibly a consequence of band bending in the perovskite layer at the maximum power point as detailed in Figure S8, Supporting Information, which is not included in the detailed balance analysis. Band bending separates the electron and hole distributions, which opposes their recombination and increases their collection as electric current. Forcing flat bands in the perovskite layer by assuming larger dielectric constants (representing for example screening by mobile ions) or thicker transport layers leads to fill factors of 0.829 and 0.821 , which are close to the detailed balance result of 0.820 .

Decreasing the mobility of the perovskite absorber to the OPTP-derived intra-grain value of $16 \text{ cm}^2 \text{ V}^{-1} \text{ s}^{-1}$ results in a small reduction of the fill factor from 0.84 to 0.82 . However, the measured JV-curve with a fill factor of 0.77 can be reproduced with an effective perovskite mobility of $5 \text{ cm}^2 \text{ V}^{-1} \text{ s}^{-1}$ and a mobility of the HTL of $10^{-3} \text{ cm}^2 \text{ V}^{-1} \text{ s}^{-1}$. The lower perovskite mobility reproduces the shunt-like loss ($R_{sh} \approx 1 \text{ k}\Omega\text{cm}^2$) at lower voltages and the reduced mobility of the transport layer reproduces the series resistance-like loss ($R_s \approx 2 \Omega\text{cm}^2$) at larger voltages. This modeling suggests that transport losses occur partially in the perovskite layer possibly due to transport barriers at grain boundaries that reduce the effective mobility

to $5 \text{ cm}^2 \text{ V}^{-1} \text{ s}^{-1}$, and partially in the HTL with insufficient mobility. This finding is in line with recent reports on improved fill-factors in very similar triple cation solar cells. Substituting the HTL by a self-assembled monolayer (SAM) increased the fill factor from 0.80 to 0.84 and led to world-record perovskite-silicon tandem solar cells with 29.15% power conversion efficiency.^[66] Substituting the perovskite material with a large-grain double cation perovskite led to a similar increase from 0.79 to 0.83 .^[67]

However, due to the large number of material properties that determine the JV-curve, the measured curve can also be reproduced with other combinations of parameters. For instance, band offset, ion diffusion, or shunts can affect the fill factor. Therefore, accurate and reproducible measurements of the material properties are mandatory for definitive conclusions. To this end, we will focus in the last section on minimizing the inter-laboratory variations in TRMC and OPTP-derived sum mobilities to provide material scientists with a reliable value and confidence interval.

6. Inter-Laboratory Variations

Large inter-laboratory variations for the mobilities in lead-halide perovskites have been highlighted in the TRMC and OPTP reviews of Savenije and Herz.^[3,4] However, it is unclear whether inter-laboratory variations or real differences between the individual samples are dominating. As the first step, here the influence of compositional variations is excluded by considering published mobilities of MAPbI_3 only. Still, variations over orders of magnitude can be observed in these mobilities in Figure 6a, which are also listed in the Note S9, Supporting Information.

To probe exclusively inter-laboratory variations, the mobility of identical samples was measured in 15 different TRMC and OPTP laboratories. For this endeavor $\text{Cs}_{0.05}(\text{FA}_{0.83}\text{MA}_{0.17})_{0.95}\text{Pb}(\text{I}_{0.83}\text{Br}_{0.17})_3$ thin films were chosen, as they are more stable than pure MAPbI_3 , in addition to pieces of an InP wafer. The results of these inter-laboratory comparisons can be seen in Figure 6a. The retrieved terahertz mobility spectra and the individual values are given in the Note S10, Supporting Information. The injection levels for these inter-laboratory comparisons were between 5×10^{11} and 5×10^{12} photons per cm^2 and pulse, close to 1 sun condition.

The standard deviation of the OPTP- and TRMC-derived mobilities increase from 5% for measurements with the same setup at the Helmholtz Zentrum Berlin before sending them to the participating laboratories, to 70% for the initial measurements in the participating laboratories, to 150% for the literature data.

The contributions to these mobility variations are disentangled in Figure 6b. The twofold increase of the standard deviation from our inter-laboratory study and to the literature survey can be attributed to different assumptions on the excitonic quantum yield and real differences between the probed samples, such as the grain size. The literature survey contains single crystals, polycrystalline thin films, and mesoporous samples with various grain sizes. Additionally, the cation composition has been reported to affect the TRMC or OPTP-derived mobility in the lead halide perovskites, but can be excluded here

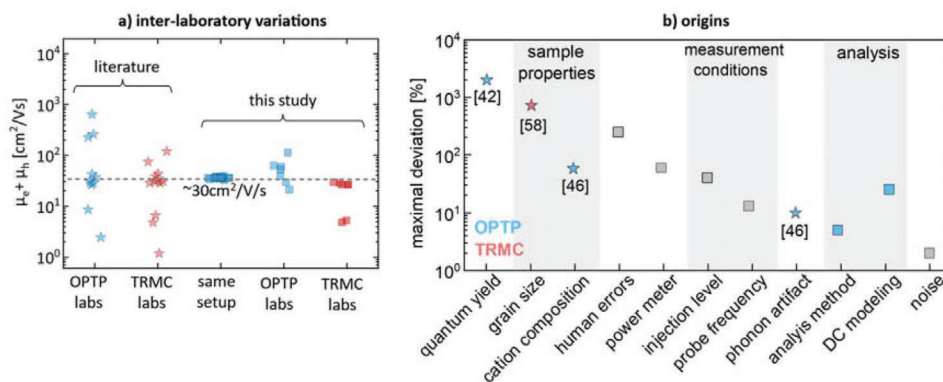


Figure 6. Variations in terahertz and microwave-derived mobilities. a) Variations of the sum mobility μ_{Σ} increase from control measurements with the same OPTP setup on $\text{Cs}_{0.05}(\text{FA}_{0.83}\text{MA}_{0.17})_{0.95}\text{Pb}(\text{I}_{0.83}\text{Br}_{0.17})_3$, over the initial measurements in the participating laboratories on $\text{Cs}_{0.05}(\text{FA}_{0.83}\text{MA}_{0.17})_{0.95}\text{Pb}(\text{I}_{0.83}\text{Br}_{0.17})_3$ to literature values of MAPbI_3 . b) Mobility variations depending on their origin. Variations marked by a star were reported in literature and were mostly excluded for this inter-laboratory comparison as the quantum yield was set to one and as the samples had the same grain size and cation composition. Our inter-laboratory variations are marked by a squared and are gained from the supporting information S11 for “human errors”, from S14 for “power meter”, from Figure 2h for “injection level”, and from Figure 4a for “probe frequency”. “analysis method” compares thin-film approximation and the transfer matrix method. “DC modelling” compares the DC-mobilities obtained by modelling TRTS mobility spectra with Drude model and with Drude-Smith model. The “noise” is the signal-to-noise ratio achieved in Figure 10a with a relatively sensitive OPTP setup.

as only MAPbI_3 was considered for the literature survey.^[47,62] All these known effects were excluded for our inter-laboratory comparison. The quantum yield was set to one because no sign of exciton formation or trapping was observed. Further, the samples came from the same deposition run, which should result in similar grain sizes and compositions.

Surprisingly, our inter-laboratory variations are rather large with a standard deviation of $\approx 70\%$. The measurements on the InP wafer exhibit similar inter-laboratory variations in Figure S11, Supporting Information. Hence, these variations seem to be material independent. The degradation of the perovskite samples was tested by 2 days of air exposure, 2 years of storage in a glove box, and 5 days of OPTP measurements, which resulted in a mobility decrease of 26 % as shown in Figure S13, Supporting Information, and is significantly harsher than the conditions during the inter-laboratory comparison. Some participating laboratories, which could store the perovskite samples appropriately, repeated their measurements. Interestingly, no common cause of the initial variations could be identified, but the worst outlier was a random human error (a forgotten filter). Also determining the induced sheet carrier concentration and variations between different power meters contributed, which are detailed in Notes S4 and S14, Supporting Information. Input parameters such as the substrate refractive index/permittivity and the reflection of the pump light (Figure S4, Supporting Information), and measurement conditions such as the injection level and the probe frequency had less influence. The occurrence of human errors may seem disappointing in natural science, but nevertheless reflects a reality not only in the field discussed in the present manuscript. To alleviate such effects, we recommend including standard samples in measurement campaigns, to provide a reliable benchmark. To raise awareness and lift your spirit by realizing that other scientists are also just human, frequent errors are listed in the Note S11, Supporting Information, (not all of them occurred during this study). If noticed, it is important to publish errata, which

proves the credibility of the author and is necessary for the fields that build on our results.

The medians of 33 and of 25 $\text{cm}^2 \text{V}^{-1} \text{s}^{-1}$ of our OPTP and TRMC measurements on $\text{Cs}_{0.05}(\text{FA}_{0.83}\text{MA}_{0.17})_{0.95}\text{Pb}(\text{I}_{0.83}\text{Br}_{0.17})_3$ are very similar to the medians of the literature values on MAPbI_3 of 31.7 and 28 $\text{cm}^2 \text{V}^{-1} \text{s}^{-1}$. This similarity of mobilities in lead-halide perovskites of different compositions is in line with a previous OPTP study.^[47] Hence, sum mobilities around 30 $\text{cm}^2 \text{V}^{-1} \text{s}^{-1}$ can be taken as representative for a large range of compositions of lead-halide perovskites.

Despite the relatively large standard deviation of $\approx 70\%$ of the initial measurements, the large number of participating laboratories narrows the 95 % confidence interval of the combined TRMC and OPTP data to 20–37 $\text{cm}^2 \text{V}^{-1} \text{s}^{-1}$. This realistic confidence interval of $\approx \pm 30\%$ is used as the error bar in Figure 4 and is clearly larger than the signal-to-noise ratios of $\approx 2\%$ in the best OPTP measurements and the sample-to-sample variations of 5 % measured in the same OPTP setup. To increase the comparability between future studies, we offer spare samples of this study for cross-calibration to TRMC and OPTP laboratories that have not participated in that study so far.

7. Conclusion

By combining the expertise of 15 TRTS and TRMC laboratories, this work attempted to provide a best practice for the interpretation of (oc)-TRMC, TRTS, and OPTP measurements on neat photovoltaic materials to precisely predict their potential performance in solar cells. It was demonstrated on lead halide perovskite, which is one of the most promising materials for future solar applications, that these techniques are complementary in their transient time windows, their probed transport lengths, and their sensitivities. OPTP can monitor fast processes such as trapping into defect states, exciton formation, or the rather strong recombination in early-stage materials, kesterites, or

CdTe. TRMC adds the slower processes such as long-living trapped carriers or weak recombination in advanced materials such as halide perovskites, Cd(Se,Te), and CIGS.

For lead-halide perovskites with modest Br or Cl content, theoretical and experimental evidence suggest that excitons do not significantly form under terrestrial solar conditions and neither affects the lifetime of charge carriers nor their mobility. The assumption of significant exciton formation was identified as the origin of the most pronounced outliers in reported mobilities of lead halide perovskites. Also trapping was not observed in our high-quality material. For such conditions, a simple phenomenological approach was presented that yields the relevant charge carrier lifetime at 1 sun conditions and the implied resistance-free JV-curve from injection-dependent (photoconductivity) transients. This analysis revealed a maximum power conversion efficiency of 24.6 % that the probed neat perovskite thin film can support in a device. To identify additional transport losses, the TRMC and TRTS derived mobility spectra were combined and interpreted in the modified Drude–Smith model. The modest sum mobilities at THz frequencies of $32 \pm 8 \text{ cm}^2 \text{ V}^{-1} \text{ s}^{-1}$ compared to InP with $2800 \text{ cm}^2 \text{ V}^{-1} \text{ s}^{-1}$ were explained by extraordinarily frequent bulk scattering, larger effective masses, and potentially microscopic localization in domain sizes below 20 nm. Such domains may be caused by crystallographic twinning or dynamic disorder, but not by the grain sizes of 200 nm that were observed by SEM. Hence, the THz-mobility was identified as intra-grain mobility. In contrast, TRMC mobilities at GHz frequencies can be reduced by typical grain sizes in halide perovskites. Similar intra-grain mobilities for electrons and holes of $16 \pm 4 \text{ cm}^2 \text{ V}^{-1} \text{ s}^{-1}$ were deduced, in good agreement with the median of previously reported values and seem to be representative for a wide range of compositions in lead halide perovskites. Such intra-grain mobilities allow modeling the JV-curve for the best case of large grains extending from front to back interface or grain boundaries that pose no transport barriers. The measured finite intra-grain mobility in perovskite limits the solar cell by slightly reducing the fill factor by 2 %. The JV-curve of the actual completed solar cell exhibited further transport losses, which were reproduced by a combination of lower effective mobility of $5 \text{ cm}^2 \text{ V}^{-1} \text{ s}^{-1}$ in the perovskite film—possibly due to grain boundaries—and an insufficient transport in the contact layers. The excellent agreement between predicted and actual performance emphasizes that the presented analysis is crucial for future accurate predictions, and we invite further laboratories to cross-calibrate their TRMC and OPTP setups with us.

While the data here were limited to InP and a lead halide perovskite, the presented techniques can guide the development of any emerging semiconductor for photovoltaic or photoelectrochemical energy conversion with high predictive power. Additional to the potential of bare photovoltaic materials, the limitations of depositing contact layers can be accessed separately.

Supporting Information

Supporting Information is available from the Wiley Online Library or from the author.

Acknowledgements

J.B.B. and M.M.T. acknowledge support from the U.S. Department of Energy's Office of Energy Efficiency and Renewable Energy (EERE) under the Solar Energy Technologies Office (SETO) Award Number DE-EE0008986. S.L., J.M.C., and S.A. acknowledge support by the U.S. National Science Foundation under CHE – 1 566 160. J.M.C. was supported by a U.S. National Science Foundation Graduate Research Fellowship under grant number DGE-1321846 and by a generous donation by the Joan Rowland Foundation. J.G.L. and M.J.H. thank the National Science Foundation for financial support (Award No. 1 942 558). M.S. thanks the Helmholtz International Research School HI-SCORE (“Hybrid Integrated Systems for Conversion of Solar Energy”) for funding and support. V.C.P. and P.K. acknowledge the Operational Programme “Research, Development and Education” financed by European Structural and Investment Funds and the Czech Ministry of Education, Youth and Sports (Project No. SOLID21-CZ.02.1.01/0.0/0.0/16_019/0000760). J.A.S. acknowledges support from the Onsager Graduate Research Fellowship in Chemistry. E.J.H. and T.J.M. acknowledge the Internal NIST22 Scientific and Technical Research and Services (STRS). M.S. and T.U. acknowledge HyPerCells a joint graduate school of the University of Potsdam and of the Helmholtz-Zentrum Berlin. M.S. and H.H. acknowledge the Deutsche Forschungsgemeinschaft (DFG, German Research Foundation) – project number 423 749 265 and 424 709 669 – SPP 2196 (SURPRISE and HIPSTER) and the Federal Ministry for Economic Affairs and Energy within the framework of the 7th Energy Research Programme (P3T-HOPE, 03EE1017C) for funding. J.N. and J.A.S. acknowledge financial support from the National Science Foundation (NSF) under grant number CHE-1954453. P.D. and V.D. thank the DFG for the support within the programme SPP2196 under DY 18/14-1. R.K. acknowledges the Grant-in-Aid for Scientific Research (No.20H02699) from the Ministry of Education, Culture, Sports, Science, and Technology of Japan. The views and opinions of authors expressed herein do not necessarily state or reflect those of the U.S. Department of Energy, U.S. National Science Foundation, or the United States Government. L.D.A.S. and M.F. obtained financial support from the research program TOP-grants with project number 715.016.002, which is financed by the Netherlands Organization for Scientific Research (NWO). Open Access funding enabled and organized by Projekt DEAL.

Conflict of Interest

The authors declare no conflict of interest.

Keywords

lifetime, microwaves, mobility, solar cells, terahertz

Received: September 7, 2021

Revised: January 11, 2022

Published online: February 26, 2022

- [1] M. A. Green, E. D. Dunlop, J. Hohl-Ebinger, M. Yoshita, N. Kopidakis, X. Hao, *Prog. Photovoltaics* **2021**, 29, 657.
- [2] M. Stollerfoht, M. Grischek, P. Caprioglio, C. M. Wolff, E. Gutierrez-Partida, F. Peña-Camargo, D. Rothhardt, S. Zhang, M. Raoufi, J. Wolansky, M. Abdi-Jalebi, S. D. Stranks, S. Albrecht, T. Kirchartz, D. Neher, *Adv. Mater.* **2020**, 32, 2000080.
- [3] T. J. Savenije, D. Guo, V. M. Caselli, E. M. Hutter, *Adv. Energy Mater.* **2020**, 10, 1903788.
- [4] L. M. Herz, *ACS Energy Lett.* **2017**, 2, 1539.

- [5] I. Levine, S. Gupta, A. Bera, D. Ceratti, G. Hodes, D. Cahen, D. Guo, T. J. Savenije, J. Ávila, H. J. Bolink, O. Milla, D. Azulay, I. Balberg, *J. Appl. Phys.* **2018**, 124, 103103.
- [6] M. Stollerfoht, C. M. Wolff, J. A. Márquez, S. Zhang, C. J. Hages, D. Rothhardt, S. Albrecht, P. L. Burn, P. Meredith, T. Unold, D. Neher, *Nat. Energy* **2018**, 3, 847.
- [7] B. Pattengale, J. Neu, S. Ostresh, G. Hu, J. A. Spies, R. Okabe, G. W. Brudvig, C. A. Schmuttenmaer, *J. Am. Chem. Soc.* **2019**, 141, 9793.
- [8] H. Hempel, T. Unold, R. Eichberger, *Opt. Express* **2017**, 25, 17227.
- [9] R. Ulbricht, E. Hendry, J. Shan, T. F. Heinz, M. Bonn, *Rev. Mod. Phys.* **2011**, 83, 543.
- [10] P. U. Jepsen, D. G. Cooke, M. Koch, *Laser Photonics Rev.* **2010**, 5, 124.
- [11] P. Kuzel, H. Nemeč, *Adv. Opt. Mater.* **2020**, 8, 1900623.
- [12] J. Neu, K. P. Regan, J. R. Swierk, C. A. Schmuttenmaer, *Appl. Phys. Lett.* **2018**, 113, 233901.
- [13] J. Neu, M. Rahm, *Opt. Express* **2015**, 23, 12900.
- [14] C. J. Hages, A. Redinger, S. Levchenko, H. Hempel, M. J. Koeper, R. Agrawal, D. Greiner, C. A. Kaufmann, T. Unold, *Adv. Energy Mater.* **2017**, 7, 1700167.
- [15] R. A. Street, *Hydrogenated amorphous silicon*, Cambridge University Press, Cambridge **2005**.
- [16] M. Maiberg, T. Hölscher, S. Zahedi-Azad, R. Scheer, *J. Appl. Phys.* **2015**, 118, 105701.
- [17] R. A. Kaindl, D. Hägele, M. A. Carnahan, D. S. Chemla, *Phys. Rev. B* **2009**, 79.
- [18] J. Lauth, M. Failla, E. Klein, C. Klinke, S. Kinge, L. D. A. Siebbeles, *Nanoscale* **2019**, 11, 21569.
- [19] A. Kulkarni, W. H. Evers, T. P. van Waas, L. D. A. Siebbeles, *J. Phys. Chem. C* **2020**, 124, 7550.
- [20] M. N. Saha, *Proc. R. Soc. London, Ser. A* **1921**, 99, 135.
- [21] D. Snoko, *Solid State Commun.* **2008**, 146, 73.
- [22] M. Baranowski, P. Plochocka, *Adv. Energy Mater.* **2020**, 10, 1903659.
- [23] D. A. Valverde-Chavez, C. S. Ponseca, C. C. Stoumpos, A. Yartsev, M. G. Kanatzidis, V. Sundström, D. G. Cooke, *Energy Environ. Sci.* **2015**, 8, 3700.
- [24] M. C. Gelvez-Rueda, E. M. Hutter, D. H. Cao, N. Renaud, C. C. Stoumpos, J. T. Hupp, T. J. Savenije, M. G. Kanatzidis, F. C. Grozema, *J. Phys. Chem. C* **2017**, 121, 26566.
- [25] V. D'Innocenzo, G. Grancini, M. J. P. Alcocer, A. R. S. Kandada, S. D. Stranks, M. M. Lee, G. Lanzani, H. J. Snaith, A. Petrozza, *Nat. Commun.* **2014**, 5, 3586.
- [26] J. Yang, X. Wen, H. Xia, R. Sheng, Q. Ma, J. Kim, P. Tapping, T. Harada, T. W. Kee, F. Huang, Y.-B. Cheng, M. Green, A. Ho-Baillie, S. Huang, S. Shrestha, R. Patterson, G. Conibeer, *Nat. Commun.* **2017**, 8, 14120.
- [27] J. E. Kroeze, T. J. Savenije, J. M. Warman, *J. Am. Chem. Soc.* **2004**, 126, 7608.
- [28] T. J. Savenije, A. Huijser, M. J. W. Vermeulen, R. Katoh, *Chem. Phys. Lett.* **2008**, 461, 93.
- [29] J. G. Labram, M. L. Chabinc, *J. Appl. Phys.* **2017**, 122, 065501.
- [30] D. Guo, V. M. Caselli, E. M. Hutter, T. J. Savenije, *ACS Energy Lett.* **2019**, 4, 855.
- [31] T. Kirchartz, L. Krückemeier, E. L. Unger, *APL Mater.* **2018**, 6, 100702.
- [32] H. Hempel, C. J. Hages, R. Eichberger, I. Repins, T. Unold, *Sci. Rep.* **2018**, 8, 14476.
- [33] F. Staub, H. Hempel, J.-C. Hebig, J. Mock, U. W. Paetzold, U. Rau, T. Unold, T. Kirchartz, *Phys. Rev. Appl.* **2016**, 6, 044017.
- [34] M. B. Johnston, L. M. Herz, *Acc. Chem. Res.* **2015**, 49, 146.
- [35] E. M. Hutter, J.-J. Hofman, M. L. Petrus, M. Moes, R. D. Abellón, P. Docampo, T. J. Savenije, *Adv. Energy Mater.* **2017**, 7, 1602349.
- [36] E. M. Hutter, G. E. Eperon, S. D. Stranks, T. J. Savenije, *J. Phys. Chem. Lett.* **2015**, 6, 3082.
- [37] T. Kirchartz, J. A. Márquez, M. Stollerfoht, T. Unold, *Adv. Energy Mater.* **2020**, 10, 1904134.
- [38] R. A. Sinton, A. Cuevas, *Proceedings of the 16th European Photovoltaic Solar Energy Conference*, James & James (Science Publishers) Ltd, London **2000**, pp. 1152.
- [39] T. L. Cocker, D. Baillie, M. Buruma, L. V. Titova, R. D. Sydora, F. Marsiglio, F. A. Hegmann, *Phys. Rev. B* **2017**, 96, 035203.
- [40] D. Tedeschi, H. A. Fonseka, E. Blundo, A. G. del Águila, Y. Guo, H. H. Tan, P. C. M. Christianen, C. Jagadish, A. Polimeni, M. D. Luca, *ACS Nano* **2020**, 14, 11613.
- [41] Y.-S. Kim, K. Hummer, G. Kresse, *Phys. Rev. B* **2009**, 80, 035203.
- [42] V. V. Galavanov, N. V. Siukaev, *Phys. Status Solidi B* **1970**, 38, 523.
- [43] C. La-o-vorakiat, T. Salim, J. Kadro, M.-T. Khuc, R. Haselsberger, L. Cheng, H. Xia, G. G. Gurzadyan, H. Su, Y. M. Lam, R. A. Marcus, M.-E. Michel-Beyerle, E. E. M. Chia, *Nat. Commun.* **2015**, 6, 7903.
- [44] M. Bonn, K. Miyata, E. Hendry, X.-Y. Zhu, *ACS Energy Lett.* **2017**, 2, 2555.
- [45] C. La-o-Vorakiat, L. Cheng, T. Salim, R. A. Marcus, M.-E. Michel-Beyerle, Y. M. Lam, E. E. M. Chia, *Appl. Phys. Lett.* **2017**, 110, 123901.
- [46] D. Zhao, H. Hu, R. Haselsberger, R. A. Marcus, M.-E. Michel-Beyerle, Y. M. Lam, J.-X. Zhu, C. La-o-Vorakiat, M. C. Beard, E. E. M. Chia, *ACS Nano* **2019**, 13, 8826.
- [47] Y. Zhai, K. Wang, F. Zhang, C. Xiao, A. H. Rose, K. Zhu, M. C. Beard, *ACS Energy Lett.* **2019**, 5, 47.
- [48] I. Anusca, S. Balčiūnas, P. Gemeiner, Š. Švirskas, M. Sanliyalp, G. Lackner, C. Fettkenhauer, J. Belovickis, V. Samulionis, M. Ivanov, B. Dkhil, J. Banys, V. V. Shvartsman, D. C. Lupascu, *Adv. Energy Mater.* **2017**, 7, 1700600.
- [49] V. M. Caselli, M. Fischer, D. Meggiolaro, E. Mosconi, F. De Angelis, S. D. Stranks, A. Baumann, V. Dyakonov, E. M. Hutter, T. J. Savenije, *J. Phys. Chem. Lett.* **2019**, 10, 5128.
- [50] K. Galkowski, A. Mitioglu, A. Miyata, P. Plochocka, O. Portugall, G. E. Eperon, J. T.-W. Wang, T. Stergiopoulos, S. D. Stranks, H. J. Snaith, R. J. Nicholas, *Energy Environ. Sci.* **2016**, 9, 962.
- [51] J. T. Devreese, A. S. Alexandrov, *Rep. Prog. Phys.* **2009**, 72, 066501.
- [52] C. Wolf, H. Cho, Y.-H. Kim, T.-W. Lee, *ChemSusChem* **2017**, 10, 3705.
- [53] M. Karakus, S. A. Jensen, F. D'Angelo, D. Turchinovich, M. Bonn, E. Canovas, *J. Phys. Chem. Lett.* **2015**, 6, 4991.
- [54] J. M. Frost, *Phys. Rev. B* **2017**, 96, 195202.
- [55] P. Prins, F. C. Grozema, J. M. Schins, L. D. A. Siebbeles, *Phys. Status Solidi B* **2006**, 243, 382.
- [56] N. Smith, *Phys. Rev. B* **2001**, 64, 155106.
- [57] H. Oga, A. Saeki, Y. Ogomi, S. Hayase, S. Seki, *J. Am. Chem. Soc.* **2014**, 136, 13818.
- [58] R. L. Milot, G. E. Eperon, H. J. Snaith, M. B. Johnston, L. M. Herz, *Adv. Funct. Mater.* **2015**, 25, 6218.
- [59] I. M. Hermes, A. Best, L. Winkelmann, J. Mars, S. M. Vorpahl, M. Mezger, L. Collins, H.-J. Butt, D. S. Ginger, K. Koynov, S. A. L. Weber, *Energy Environ. Sci.* **2020**, 13, 4168.
- [60] M. J. Schilcher, P. J. Robinson, D. J. Abramovitch, L. Z. Tan, A. M. Rappe, D. R. Reichman, D. A. Egger, *ACS Energy Lett.* **2021**, 6, 2162.
- [61] H. Hempel, A. Redinger, I. Repins, C. Moisan, G. Larramona, G. Dennler, M. Handberg, S. F. Fischer, R. Eichberger, T. Unold, *J. Appl. Phys.* **2016**, 120, 175302.
- [62] O. G. Reid, M. Yang, N. Kipidakis, K. Zhu, G. Rumbles, *ACS Energy Lett.* **2016**, 1, 561.
- [63] C. Q. Xia, J. Peng, S. Poncé, J. B. Patel, A. D. Wright, T. W. Crothers, M. U. Rothmann, J. Borchert, R. L. Milot, H. Kraus, Q. Lin, F. Giustino, L. M. Herz, M. B. Johnston, *J. Phys. Chem. Lett.* **2021**, 12, 3607.
- [64] A. F. Mayadas, M. Shatzkes, *Phys. Rev. B* **1970**, 1, 1382.
- [65] M. Burgelman, P. Nollet, S. Degraeve, *Thin Solid Films* **2000**, 361, 527.
- [66] A. Al-Ashouri, E. Köhnen, B. Li, A. Magomedov, H. Hempel, P. Caprioglio, J. A. Márquez, A. B. M. Vilches, E. Kasparavicius,

J. A. Smith, N. Phung, D. Menzel, M. Grischek, L. Kegelmann, D. Skroblin, C. Gollwitzer, T. Malinauskas, M. Jošt, G. Matič, B. Rech, R. Schlatmann, M. Topič, L. Korte, A. Abate, B. Stannowski, D. Neher, M. Stolterfoht, T. Unold, V. Getautis, S. Albrecht, *Science* **2020**, 370, 1300.

[67] E. Gutierrez-Partida, H. Hempel, S. Caicedo-Dávila, M. Raoufi, F. Peña-Camargo, M. Grischek, R. Gunder, J. Diekmann, P. Caprioglio, K. O. Brinkmann, H. Köbler, S. Albrecht, T. Riedl, A. Abate, D. Abou-Ras, T. Unold, D. Neher, M. Stolterfoht, *ACS Energy Lett.* **2021**, 6, 1045.